

# Preflight Evaluation of the Performance of the Chinese Environmental Trace Gas Monitoring Instrument (EMI) by Spectral Analyses of Nitrogen Dioxide

Chengxin Zhang<sup>1</sup>, Cheng Liu<sup>1</sup>, Yang Wang<sup>1</sup>, Fuqi Si, Haijin Zhou, Minjie Zhao, Wenjing Su, Wenqiang Zhang, Ka Lok Chan, Xiong Liu, Pinhua Xie, Jianguo Liu, and Thomas Wagner

**Abstract**—The Environmental trace gas Monitoring Instrument (EMI) onboard the Chinese high-resolution remote sensing satellite GaoFen-5 is an ultraviolet–visible imaging spectrometer, aiming to quantify the global distribution of tropospheric and stratospheric trace gases and planned to be launched in spring 2018. The preflight calibration phase is essential to characterize the properties and performance of the EMI in order to provide information for data processing and trace gas retrievals. In this paper, we present the first EMI measurement of nitrogen dioxide (NO<sub>2</sub>) from a gas absorption cell using scattered sunlight as the light source by the differential optical absorption spectroscopy technique. The retrieved NO<sub>2</sub> column densities in the UV and Vis wavelength ranges are consistent with the column density in

the gas cell calculated from the NO<sub>2</sub> mixing ratio and the length of the gas cell. Furthermore, the differences of the retrieved NO<sub>2</sub> column densities among the adjoining spatial rows of the detector are less than 3%. This variation is similar to the well-known “stripes-pattern” of the Ozone Monitoring Instrument and is probably caused by remaining systematic effects like a nonperfect description of the individual instrument functions. Finally, the signal-to-noise ratios of EMI in-orbit measurements of NO<sub>2</sub> are estimated on the basis of on-ground scattered sunlight measurements and radiative transfer model simulations. Based on our results, we conclude that the EMI is capable of measuring the global distribution of the NO<sub>2</sub> column with the retrieval precision and accuracy better than 3% for the tested wavelength ranges and viewing angles.

**Index Terms**—Differential optical absorption spectroscopy (DOAS), NO<sub>2</sub>, remote sensing, satellite, spectral analysis, trace gases.

## I. INTRODUCTION

GLOBAL monitoring of atmospheric trace gas distributions from a number of ultraviolet–visible (UV–Vis) spaceborne spectrometers including GOME, SCIAMACHY, Ozone Monitoring Instrument (OMI), and GOME-2 [3]–[7] has been playing an important role in studies of atmospheric chemistry, air pollution, and climate change. Recently, these observations have been used to estimate the emission of pollutants [8]–[11], to validate model simulations [12], [13], and to support operational services such as UV forecasts and air quality forecasts [15], [16].

In order to measure global distributions of tropospheric and stratospheric trace gases (e.g., NO<sub>2</sub>, O<sub>3</sub>, HCHO, and SO<sub>2</sub>), the Environmental trace gas Monitoring Instrument (EMI) was developed by the Anhui Institute of Optics and Fine Mechanics (AIOFM), Chinese Academy of Sciences, Hefei, China, and is planned to be launched in spring 2018 onboard the Chinese high-resolution remote sensing satellite GaoFen-5, which will fly in a sun-synchronous polar orbit with an ascending equatorial crossing time of 1:30 P.M. EMI is a nadir-viewing push broom spectrometer, designed to provide these atmospheric measurements with a daily global coverage.

The differential optical absorption spectroscopy (DOAS) technique based on Beer–Lambert law has been widely used to retrieve slant column density (SCD) of several trace gases from ground-based, mobile, airborne, and satellite measurements

Manuscript received August 12, 2017; revised December 15, 2017; accepted January 23, 2018. This work was supported in part by the National High-Resolution Earth Observation Project of China under Grant 05-Y20A16-9001-15/17-2, in part by the National Key Project of MOST under Grant 2016YFC0203302, in part by the National Natural Science Foundation of China under Grant 41575021, Grant 91544212, and Grant 41405117, and in part by the Key Project of CAS under Grant KJZD-EW-TZ-G06-01. (Chengxin Zhang and Cheng Liu contributed equally to this work.) (Corresponding authors: Cheng Liu and Yang Wang.)

C. Zhang and W. Su are with the School of Earth and Space Sciences, University of Science and Technology of China, Hefei 230026, China (e-mail: zcx2011@mail.ustc.edu.cn; swj1993@mail.ustc.edu.cn).

C. Liu is with the School of Earth and Space Sciences, University of Science and Technology of China, Hefei 230026, China, with the Anhui Institute of Optics and Fine Mechanics, Chinese Academy of Sciences, Hefei 230031, China, with the Center for Excellence in Regional Atmospheric Environment, Institute of Urban Environment, Chinese Academy of Sciences, Xiamen 361021, China, and also with the Anhui Province Key Laboratory of Polar Environment and Global Change, University of Science and Technology of China, Hefei 230026, China (e-mail: chliu81@ustc.edu.cn).

Y. Wang and T. Wagner are with the Max Planck Institute for Chemistry, 55128 Mainz, Germany (e-mail: y.wang@mpic.de; thomas.wagner@mpic.de).

F. Si, H. Zhou, and M. Zhao are with the Anhui Institute of Optics and Fine Mechanics, Chinese Academy of Sciences, Hefei 230031, China (e-mail: sifuqi@aiofm.ac.cn; hjzhou@aiofm.ac.cn; mjzhao@aiofm.ac.cn).

W. Zhang is with the School of Environmental Science and Optoelectronic Technology, University of Science and Technology of China, Hefei 230026, China (e-mail: zwq16@mail.ustc.edu.cn).

K. L. Chan is with Ludwig-Maximilians-Universität München, 80539 Munich, Germany (e-mail: lok.chan@lmu.de).

X. Liu is with the Harvard-Smithsonian Center for Astrophysics, Cambridge, MA 02144 USA (e-mail: xliu@cfa.harvard.edu).

P. Xie and J. Liu are with the Anhui Institute of Optics and Fine Mechanics, Chinese Academy of Sciences, Hefei 230031, China, and also with the Center for Excellence in Regional Atmospheric Environment, Institute of Urban Environment, Chinese Academy of Sciences, Xiamen 361021, China (e-mail: phxie@aiofm.ac.cn; jgliu@aiofm.ac.cn).

Color versions of one or more of the figures in this paper are available online at <http://ieeexplore.ieee.org>.

Digital Object Identifier 10.1109/TGRS.2018.2798038

in the UV, Vis, and near-infrared ranges [18]. In this paper, the DOAS technique is applied to laboratory measurements of the EMI using scattered sunlight as the source. The light traverses a gas cell filled with nitrogen dioxide ( $\text{NO}_2$ ) before it is recorded by the EMI during the experiment. From the measured spectra, the  $\text{NO}_2$  absorption is analyzed in the UV and Vis wavelength ranges. From this experiment, the quantitative performance of the DOAS approach for the EMI is evaluated. Similar studies have been done for other satellite instruments. Measuring absorption cross sections of trace gases in a cell at various pressures and temperatures was performed using a Xenon lamp for GOME [19], [20], SCIAMACHY [23], and GOME-2 [25] before launch. Measurements of trace gases in a cell using a lamp and those in the atmosphere using scattered sunlight in the zenith view were performed for the OMI instrument with the DOAS retrieval approach [26]. It was found that the derived cross sections of trace gases compare quite well with those derived from the convolution of the literature high-resolution cross sections with the accurately measured OMI slit function [27].

By using a similar approach, scattered sunlight measurements of  $\text{NO}_2$  in a gas absorption cell are performed with the EMI to explicitly consider the solar Fraunhofer lines in the DOAS fit and to characterize the ability of EMI to retrieve  $\text{NO}_2$  SCD in orbit. Due to the known  $\text{NO}_2$  concentration in the gas cell and the large field of view (FOV) of EMI, the spatial row dependence can be characterized from the retrieved  $\text{NO}_2$  SCDs. This study is motivated by the known cross-track striping pattern of the  $\text{NO}_2$  SCDs retrieved from a typical 2-D detector such as OMI, which is attributed to the imperfect cross-track calibration [28]. Furthermore, the instrumental signal-to-noise ratio (SNR) of the scattered sunlight measurements is characterized for EMI and transformed to the in-orbit SNR by the use of radiative transfer model (RTM) simulations.

This paper is organized as follows. First, the EMI and the preflight calibration are described in Section II. Afterward, the  $\text{NO}_2$  DOAS retrieval from the laboratory spectral measurements by the EMI is given in Section III. And an estimation of EMI SNR is given in Section IV. Finally, the summary and conclusion are given in Section V.

## II. DESCRIPTION OF THE EMI

### A. Environmental Trace Gas Monitoring Instrument

The EMI is a satellite UV-Vis spectrometer, which is designed to measure earthshine radiances and solar irradiances in the wavelength range of 240–710 nm at a moderate spectral resolution [full width at half maximum (FWHM)] of 0.3–0.5 nm (depending on wavelength and viewing angle). The EMI adopts Offner imaging spectrometer [29] with four spectral channels, and each channel uses a 2-D (spectral and spatial) CCD detector, which enables an FOV of  $114^\circ$  and  $0.5^\circ$  in the swath and flight directions, respectively. The four spectral channels cover the following wavelength ranges: 240–315, 311–403, 401–550, and 545–710 nm for the UV1, UV2, VIS1, and VIS2 channels, respectively. Fig. 1(a) illustrates the optical layout of the EMI

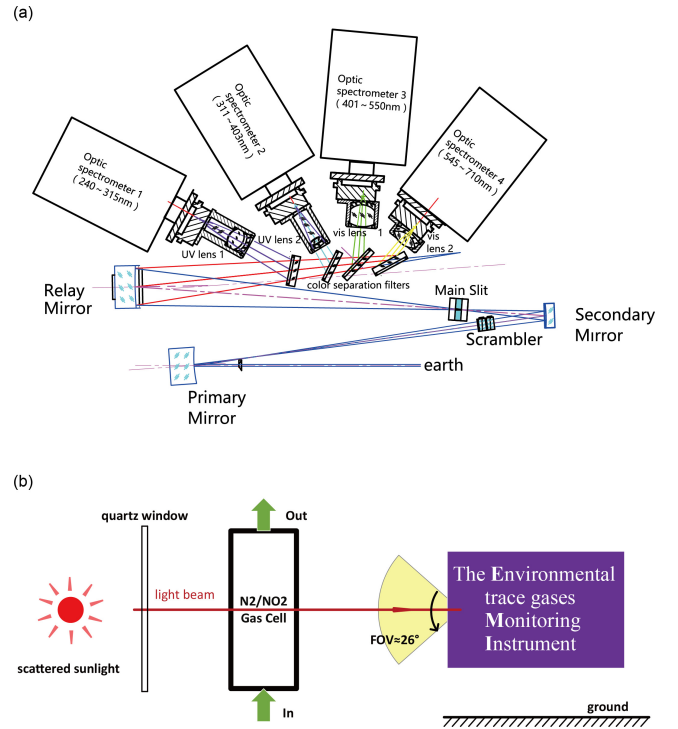


Fig. 1. (a) Optical layout of the EMI fore-optics system, and the Offner convex grating imaging spectrometer. (b) Schematic of the experimental setup.

fore-optics system and the Offner convex grating imaging spectrometer.

In the EMI operational mode of earthshine radiance measurements, the typical exposure time of individual measurements varies from 0.5 to 2 s, depending on the spectral channels and measurement latitudes, in order to reach an optimal saturation level of the CCD detectors. Individual radiance measurements during the measurement period of 2 s are co-added in the level 0–1b data processing phase, leading to an effective integration time of 2 s for each spectrum. The binning of spatial rows is applied to improve the SNR, i.e., 43 binned rows for the UV (UV1 and UV2) channels and 48 binned rows for the VIS (VIS1 and VIS2) channels. Therefore, the resulting ground pixel sizes at exact nadir position for the UV and VIS channels are  $43 \text{ km} \times 13 \text{ km}$  (swath direction  $\times$  flight direction) and  $37 \text{ km} \times 13 \text{ km}$ , respectively. The detailed properties of the EMI are shown in Table I.

### B. EMI Preflight Calibration

In order to derive the instrumental parameters which are needed to implement the level 0–1b processing as well as to perform the spectral retrievals, a high-quality preflight calibration phase is essential. For the EMI during this phase, the following activities were performed: wavelength calibration, radiometric calibration, slit function characterization, stray light suppression, diffuser feature measurements, etc. An overview of the calibration work is as follows.

- 1) *Wavelength Calibration*: Highly structured Fraunhofer lines of atmospheric scattered light are often used to perform wavelength calibration [30], which has been

TABLE I  
INSTRUMENTAL PROPERTIES OF THE EMI

Spectral channels	UV1: 240-315nm
	UV2: 311-403nm
	VIS1: 401-550nm
	VIS2: 545-710nm
Spectral resolution	0.3-0.5nm
Telescope swath FOV	114 degrees
Telescope flight FOV	0.5 degrees
CCD detectors	UV1/2: 1072 × 1032 (spectral × spatial) pixels
	VIS1/2: 1286 × 576 (spectral × spatial) pixels
Integration time	2s
Ground pixel size <sup>a</sup> (at exact nadir)	UV1/2: 43km × 13km (swath direction × flight direction)
	VIS1/2: 37km × 13km (swath direction × flight direction)
Mass	95kg
Size	50cm × 36cm × 65cm
Orbit	Polar, sun-synchronous
	Average altitude: 705km
	Orbit period: 98 minutes 53 seconds
	Ascending node equator crossing time: 13:30 PM
Anticipated lifetime	8 Years

<sup>a</sup> The pixel size in flight dimension didn't include the FOV.

done for the EMI during the prelaunch phase. This method will be applied to in-orbit wavelength calibration within DOAS analysis by using solar irradiance spectra.

- 2) *Radiometric Calibration*: An integrating sphere uniform source system (Labsphere type US-200-SF) is used to derive the radiometric calibration parameters, such as the pixel response nonuniformity correction parameters and the absolute radiance conversion factor [31].
- 3) *Instrument Slit Function*: A PtCrNe hollow cathode lamp is also used to characterize the EMI slit function. A Gaussian function is fit to individual lines at certain wavelengths, and the corresponding key parameters such as FWHM are derived. In-orbit variability of EMI slit function could also be parameterized by various function forms such as super-Gaussian [32], by fitting solar irradiance spectra with structured Fraunhofer lines.
- 4) *Stray Light*: Mechanisms including a light shield and other baffles have been developed to suppress the stray light. The spectral stray light was measured by the use of edge pass filter, and then compared with optical model simulations during the prelaunch phase.
- 5) *Diffuser Features*: Both the aluminum diffuser and the quartz volume diffuser are used to introduce solar irradiance into the EMI entrance optics, but they are used for different purposes. The aluminum diffuser is used for the weekly radiometric calibration, while the quartz volume diffuser is used to measure the daily

solar reference spectrum. The hemispheric reflectance and bidirectional reflectance distribution function of the diffusers are measured to ensure radiometric calibration accuracy, as described in [33].

### III. NO<sub>2</sub> GAS CELL MEASUREMENTS

#### A. Experimental Setup

The NO<sub>2</sub> absorption in a cell was measured with the EMI using scattered sunlight at ambient pressure (about 1 atm) and temperature (about 293 K) in the laboratory (located at 31.91° N, 117.16° E, and an altitude of 20 m above the ground) of AIOFM, from 11 A.M. to 11:30 A.M. on February 13, 2017. The main objective of the experiment is to evaluate the instrument performance with natural sunlight as light source.

A 40 cm × 50 cm quartz window was inlaid in the wall of the laboratory, and an 8-cm-long quartz cell was continuously flushed with either NO<sub>2</sub> gas or N<sub>2</sub> gas. The NO<sub>2</sub> gas is taken from a gas bottle with an approximate mixing ratio of 710 parts per million and then flows through a plastic pipe to the gas cell at a stable flow rate of 7.5 L/min. The EMI received the scattered sunlight passing through the window of the laboratory and the cell in horizontal direction. Due to the large FOV of the instrument and the limited width of the window, only the CCD pixels in the most central viewing direction, i.e., within an FOV of about 26° (about eight and ten binned CCD rows for UV2 and VIS1 channels, respectively) are illuminated. In the experiment, N<sub>2</sub> was first flushed into the gas cell for several minutes to eliminate all other gases remaining in the cell, and then NO<sub>2</sub> was flushed into the cell. Meanwhile, the EMI continuously recorded spectra in the UV2 and VIS1 channels during the gas flushing process. The schematic of the experimental setup is shown in Fig. 1(b).

#### B. Spectral Analyses

One important advantage of the DOAS method is that effects of scattering (e.g., Rayleigh and Mie scattering) are considered by a broadband polynomial in the spectral analysis. Therefore, knowledge about the exact amount and type of scatterers is not necessary. The absorption of the atmospheric absorbers in the measured NO<sub>2</sub> spectra (with the gas cell filled with NO<sub>2</sub>) is compensated for by using N<sub>2</sub> reference spectra (with the gas cell filled with N<sub>2</sub>), which are measured at the same geometry and at the closest time.

The obtained EMI raw spectra are analyzed with the QDOAS (version 2.111) software package [34]. The spectral fitting window of NO<sub>2</sub> is 338–370 nm for the UV2 channel and 435–490 nm for the VIS1 channel. The spectral ranges were chosen according to the wavelength coverage of the EMI, and based on the experience gained in previous studies during the CINDI [35], [36] and MAD-CAT ([http://joseba.mpg.de/mad\\_analysis.htm](http://joseba.mpg.de/mad_analysis.htm)) campaigns. A NO<sub>2</sub> cross section at 298 K [1] with solar I<sub>0</sub> correction [21], a ring spectrum calculated from the SAO2010 solar irradiance reference spectrum [14], and an additional ring spectrum as described in [17] are included in the DOAS fit. The logarithm of the ratio of the two measured spectra for the light beams passing



TABLE II  
NO<sub>2</sub> DOAS Fit SETTINGS

Parameter	Setting
Spectral fitting window	UV2: 338-370nm VIS1: 435-490nm
NO <sub>2</sub> cross-section	Vandaele et al., 1998, 298 K, I <sub>0</sub> -corrected <sup>a</sup> (10 <sup>17</sup> molecules/cm <sup>2</sup> ) [1]
Ring spectrum	Ring spectrum calculated based on the SAO2010 solar atlas [14] and a Ring spectrum scaled by (λ/354 nm) <sup>4</sup> [17]
Polynomial	5th-order
Fraunhofer reference	N <sub>2</sub> spectrum (averaged in 1min)
Wavelength calibration	Calibration based on the Fraunhofer lines of the SAO2010 solar atlas [14]

<sup>a</sup>Solar I<sub>0</sub> correction [21]

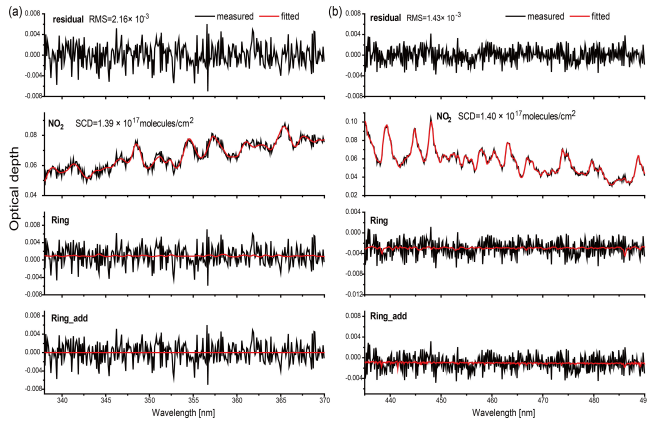


Fig. 2. DOAS fit results of NO<sub>2</sub> in the (a) UV2 and (b) VIS1 wavelength ranges. The black and red curves represent the measured and fit optical depths, respectively.

through the cell either with N<sub>2</sub> or NO<sub>2</sub> is fit by the above-mentioned cross sections convolved with the EMI slit function and a fifth-order polynomial according to

$$\ln \left[ \frac{I_{N_2}(\lambda)}{I_{NO_2}(\lambda)} \right] = \sigma_{NO_2}(\lambda) S_{NO_2} + P(\lambda) + R(\lambda) + R_{add}(\lambda). \quad (1)$$

Here,  $\sigma_{NO_2}(\lambda)$  is the absorption cross section of NO<sub>2</sub>,  $S_{NO_2}$  is the SCD of NO<sub>2</sub>,  $P(\lambda)$  represents the polynomial, and  $I_{N_2}(\lambda)$  and  $I_{NO_2}(\lambda)$  are the measured spectra for the light beams passing either through the cell with N<sub>2</sub> or NO<sub>2</sub>, respectively. The N<sub>2</sub> reference spectra are selected for each individual spatial CCD row, and wavelength shift was allowed in the DOAS fit, in order to minimize the effects of slightly different spectral properties of the different rows. The last two terms on the right-hand side of (1) account for the ring effect. Sensitivity tests show that inclusion of one or two ring spectra has only a very small effect on the results of DOAS analysis (see Appendix A). The detailed fit settings and parameters are listed in Table II. Examples of the DOAS fits of NO<sub>2</sub> in both spectral ranges are shown in Fig. 2.

### C. Discussion on the Fit Results

Based on the NO<sub>2</sub> mixing ratio and the length of cell, the NO<sub>2</sub> SCD is estimated as  $(1.40 \pm 0.07) \times 10^{17}$  molecules/cm<sup>2</sup>.

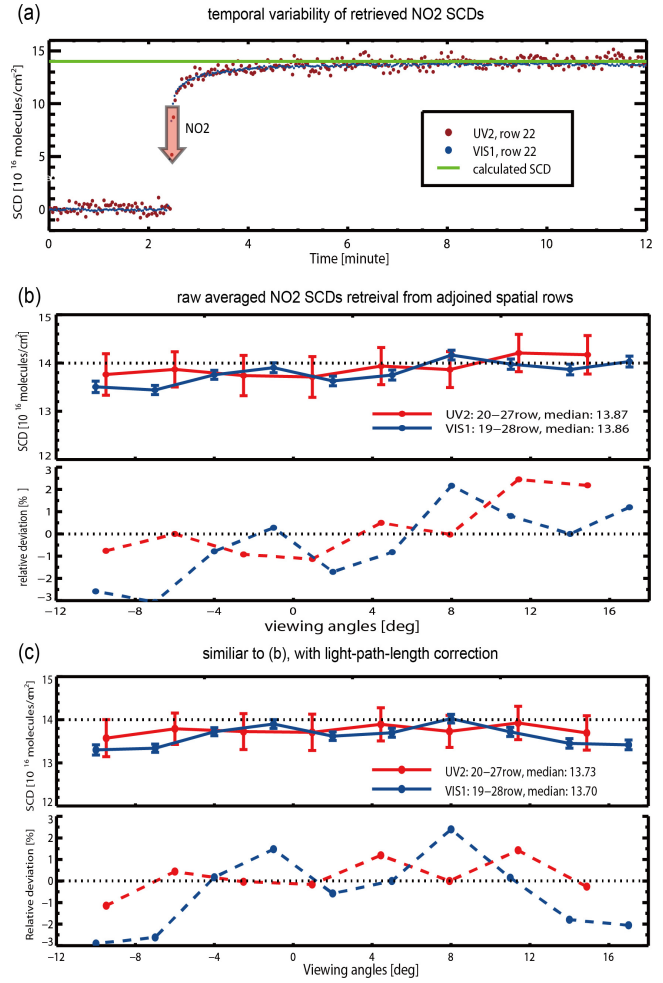


Fig. 3. Temporal and spatial (row dependent) variabilities of the retrieved NO<sub>2</sub> SCDs. (a) Time series of NO<sub>2</sub> SCDs from the central CCD rows in the UV2 (red dots) and VIS1 (blue dots) channels during the gas flushing process. During the first 2.5 min, N<sub>2</sub> was flushed into the cell, and after that period NO<sub>2</sub> was flushed into the cell. The solid green line represents the calculated NO<sub>2</sub> SCD based on the length of the cell and the NO<sub>2</sub> volume mixing ratios in the cell. (b) and (c) Averaged NO<sub>2</sub> SCDs from different CCD rows in the UV2 (red) and VIS1 (blue) channels during the steady-state period. The results before and after the light-path correction are shown. (Top and bottom) Averaged NO<sub>2</sub> SCDs and the relative deviation of NO<sub>2</sub> SCDs from the median values for individual spatial rows, respectively.

The uncertainty arises from the uncertainties of the NO<sub>2</sub> mixing ratio and the fact that the gas cell was operated under ambient conditions in the laboratory without pressure and temperature control. To estimate the time needed to completely fill the gas cell, the temporal evolution of the retrieved NO<sub>2</sub> SCDs from the central CCD rows in the UV2 and VIS1 channels during the gas flushing process was investigated [see Fig. 3(a)]. It is found that the NO<sub>2</sub> SCDs reach a steady state after the first 3 min of NO<sub>2</sub> flushing, i.e., within the time interval between 6 and 12 min of the timescale shown in Fig. 3(a). During that period, the relative standard deviation (SD) of the retrieved NO<sub>2</sub> VCD is 3% for the UV2 and 1% for the VIS1 channels, respectively. The derived average NO<sub>2</sub> SCDs with fitting uncertainties in the steady-state stage are  $(1.39 \pm 0.04) \times 10^{17}$  molecules/cm<sup>2</sup> in the UV2 channel and  $(1.37 \pm 0.01) \times 10^{17}$  molecules/cm<sup>2</sup> in the VIS1 channel, respectively. The slight differences (smaller than 2%)



among the SCDs retrieved in both channels and the calculated value indicate an excellent performance of the EMI NO<sub>2</sub> measurements.

The NO<sub>2</sub> SCDs retrieved from the individual spatial rows of the EMI are averaged during the steady-state period to reduce the random noise and are shown in Fig. 3(b). The results indicate a systematic dependence of the NO<sub>2</sub> SCDs on the spatial rows. Considering that the light path in the cell is slightly different for different spatial rows, the NO<sub>2</sub> SCDs are corrected using a geometric equation, i.e., by multiplying the SCDs by the cosine of the viewing angle of each spatial row [see Fig. 3(c)]. The results indicate that the variability of the corrected NO<sub>2</sub> SCDs for different spatial rows is less than 3% in general, while after the geometric light-path correction, the same values should be obtained for all rows. The relative deviations increase toward the edges of the rows, as shown in Fig. 3(c), which may be partly due to the lower transmission of the quartz window (i.e., lower observed intensity) for larger viewing angles. The remaining spatial row dependence of the retrieved NO<sub>2</sub> SCDs can probably be attributed to the imperfect cross-track (i.e., spatial-row-dependent) calibration of the instrument such as wavelength calibration, determination of the slit function, as well as dark current, offset, and stray light correction. Slight contributions might also arise from variations of the atmospheric NO<sub>2</sub> absorption, small differences between the solar zenith angle (SZA) of the N<sub>2</sub> reference spectrum and the NO<sub>2</sub> spectrum, and a slight variation of the NO<sub>2</sub> concentration in the cell. A similar effect has been found for typical 2-D CCD instruments, e.g., OMI, and results in a pattern of cross-track “stripes” as described in [26]. The spatial row dependence of the NO<sub>2</sub> SCDs for the EMI found in this experiment is in the similar range as the cross-track “stripes” of the DOMINO v2.0 OMI NO<sub>2</sub> products (within  $1.5 \times 10^{15}$  molecules/cm<sup>2</sup>) [37]. A destriping algorithm is currently applied to the published OMI NO<sub>2</sub> product based on the biases estimated from a cross-track variation of the retrieved raw SCDs [37]–[39]. The spatial row dependence of NO<sub>2</sub> SCDs characterized in this paper could be used to estimate the general magnitude of cross-track “stripes” of the future in-orbit EMI NO<sub>2</sub> products, although there is missing information toward the edges of the swath.

#### IV. ESTIMATION OF EMI SNR

SNR is a main constraint for the detection limit of the trace gas retrievals from satellite UV–Vis spectra [18], and significantly impacts the quality of the level 2 data products, especially for the weaker absorbers, such as SO<sub>2</sub> and HCHO. Therefore, the SNR of the EMI was characterized using two methods in this section, referred to as method 1 and method 2. Method 1 is based on the scattered sunlight measurements and radiative transfer simulations, while method 2 is based on the instrument specifications and the photon noise assumption.

##### A. Method 1

The SNR can be derived from the random structures in the NO<sub>2</sub> fit residuals. For that purpose, we determined the SDs of the fit residuals at each wavelength for all measured spectra

during the steady-state period. The resulting SDs for different spatial rows on the CCD detectors of the UV2 and VIS1 channels are shown in Fig. 4(a). Similar spectral structures of the residual SDs are found for the adjoined spatial rows, which are mainly caused by the spectral variation of the measured spectra. The reciprocal of the residual SDs represents the instrumental SNR, which is in the range of  $\sim 600$ – $800$  for the UV2 channel and  $\sim 1000$ – $1400$  for the VIS1 channel. Note that the measurements performed here were made at an almost horizontal elevation angle, for which the observed radiances are typically lower compared with those of a nadir-viewing satellite instrument. Therefore, the derived SNR is not fully representative for in-orbit measurements of EMI. According to the fact that random noise is proportional to the square root of the measured photoelectrons (UV–Vis spectrometers are typically photon shot noise limited, see Appendix B), the in-orbit EMI SNR could be estimated using the following equation:

$$\text{SNR}_{\text{sat}} = \text{SNR}_{\text{gb}} \times \sqrt{\frac{R_{\text{sat}}}{R_{\text{gb}}}}. \quad (2)$$

Here,  $\text{SNR}_{\text{gb}}$  is the EMI SNR derived from the experiment, and  $R_{\text{gb}}$  and  $R_{\text{sat}}$  refer to the radiances from the ground-based horizontal measurement and the satellite measurement, respectively. In order to evaluate the EMI in-orbit SNR,  $R_{\text{gb}}$  and  $R_{\text{sat}}$  are acquired from simulations with the vector linearized discrete ordinate radiative transfer model (VLIDORT) [40]. Note that since the radiometric calibration parameters were not yet available for the EMI sample version used in this experiment, we used simulated  $R_{\text{gb}}$  in (2) rather than calibrated measured radiances. The evaluation is expected to be representative for typical in-orbit conditions since the configuration of the experiment is the same as the typical in-orbit measurement settings, such as row binning and exposure time.

In the RTM simulations of  $R_{\text{gb}}$ , an ozone profile from OMI [24], an aerosol optical depth (AOD) of 0.5 at 550 nm from MODIS [22], and the corresponding solar and viewing geometries are used as input parameters. The aerosol profile is averaged from LiDAR measurements (hosted by AIOFM) during noon time of typical sunny winter days in December 2014 at the top of the laboratory. Note that the LiDAR profile was scaled by a MODIS-observed AOD of 0.5 at 550 nm (see Appendix C). In order to estimate the EMI in-orbit SNR at different latitudes, we simulated  $R_{\text{sat}}$  for different typical geometries and surface albedo, which can be reasonably derived from the OMI L1b data due to the similar orbital and instrumental properties of the OMI and EMI (see Table III for details). The simulated radiances for  $R_{\text{gb}}$  and  $R_{\text{sat}}$  are shown in Fig. 4(b).

$R_{\text{sat}}$  is simulated for EMI measurements over three Chinese cities in August (i.e., with different SZAs), and afterward  $\text{SNR}_{\text{sat}}$  is calculated based on (2); the SNR results are shown in Fig. 4(c). The  $\text{SNR}_{\text{sat}}$  varies slightly with wavelength and SZA, within the range of  $\sim 1000$ – $1400$  for the UV2 channel and  $\sim 1100$ – $1800$  for the VIS1 channel. However, it should be noted that the model simulations of  $R_{\text{gb}}$  might be not fully representative for the real measurements

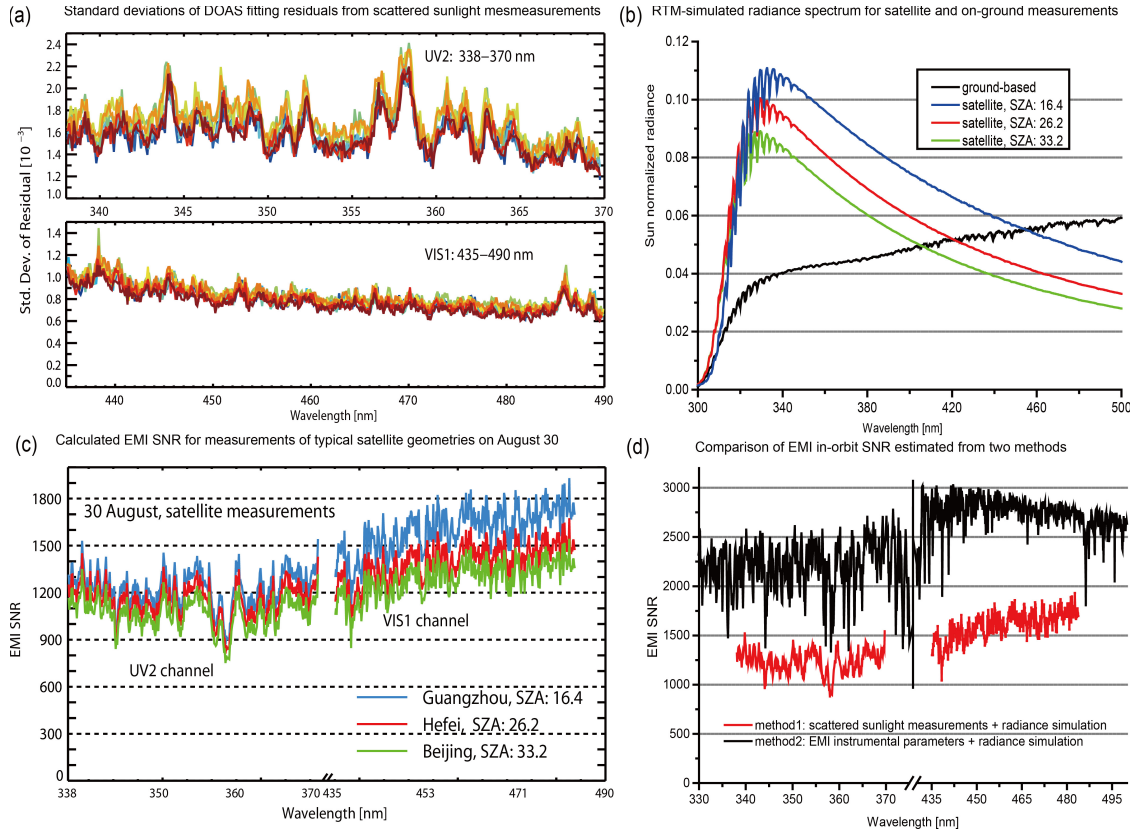


Fig. 4. Estimation of the EMI SNR of in-orbit NO<sub>2</sub> measurements. (a) Wavelength-dependent SDs of the NO<sub>2</sub> fit residuals for the measurements in the (Top) UV2 and (Bottom) VIS1 channels, during the steady-state period of the NO<sub>2</sub> flushing process. Different colors represent the results for individual spatial rows on the CCD detectors. (b) Normalized radiances simulated by the VLIDORT model for the ground-based scattered sunlight measurements ( $R_{gb}$ ) in black line and the satellite measurements ( $R_{sat}$ ). The different colors represent different SZAs. (c) In-orbit EMI SNR estimated for measurements over three Chinese cities based on the SNR derived in (a) and the radiances simulated by the VLIDORT model in (b). The three cities are Guangzhou (22.6° N), Hefei (31.5° N), and Beijing (39.5° N). (d) Comparison of in-orbit EMI SNRs calculated by two methods on the basis of (2) and (3). The results from method 1 and method 2 are shown by red and black lines, respectively.

TABLE III  
INPUT PARAMETERS OF VLIDORT RADIANCE SIMULATIONS

Input parameters	$R_{gb}$ simulation	$R_{sat}$ simulation
Surface albedo	0.075, from OMI [2]	Using OMI solar
Solar zenith angle	47.0	and viewing
Viewing zenith angle	89.9	geometry, and OMI
Relative azimuth angle	149.14	albedo at central
		wavelengths of the
		UV2 and VIS1
		fitting ranges [2]
Aerosol information	An AOD of 0.5 at 550nm from MODIS [22], and LiDAR-observed profile shape (See Appendix C)	None
Trace gases profiles	OMI ozone profile [24], simulated NO <sub>2</sub> profile by WRF-chem	OMI ozone profile [24]

made at an almost horizontal elevation angle. Also, the local aerosol conditions might be different from the input derived from MODIS measurements. Sensitivity tests show that the model results probably overestimate the true radiance observed by the instrument by up to 40% (based on the horizon scan measurements of a MAX-DOAS instrument during the CINDI-2 campaign [41]). Such an overestimation would

account for a 15% underestimation of the EMI in-orbit SNR based on the scattered light observations.

### B. Method 2

In addition to the determination of the SNR based on the method described above, the SNR was also determined by another method based on the direct estimation of the photoelectron counts received by a single binned pixel of the EMI CCD detector

$$\text{SNR}_{\text{sat}} = \frac{\text{Signal}}{\text{Noise}} \approx \sqrt{\text{Signal}} = \sqrt{R_{\text{sat}} \times t \times s \times a \times w \times \tau}. \quad (3)$$

Here,  $R_{\text{sat}}$  is the simulated radiance for satellite geometry in units of photons/s/cm<sup>2</sup>/sr/nm, and  $t$ ,  $s$ ,  $a$ ,  $w$ , and  $\tau$  are EMI parameters, namely, integration time (2 s), telescope entrance area size (0.0308 cm<sup>2</sup>), solid angle for a single pixel (about 0.0005 sr), wavelength interval for a single pixel (0.095 nm for UV2 channel, and 0.123 nm for VIS1 channel), and the combined system optical throughput and quantum efficiency (about 0.092), respectively. The comparison results of the two methods based on the same simulated radiance for satellite geometry ( $R_{\text{sat}}$ ) are shown in Fig. 4(d). The EMI SNR results using method 2 are significantly higher than those using method 1, which is probably caused by neglecting other

(instrumental) sources of noise by method 2 and a possible underestimation of the SNR by method 1.

## V. CONCLUSION

Measurements of the  $\text{NO}_2$  absorption in a gas cell using scattered sunlight are performed with the EMI, which is designed for the Chinese high-resolution remote sensing satellite GaoFen-5. The main aim of this experiment was to explicitly evaluate the quality of the  $\text{NO}_2$  DOAS retrievals in the UV and Vis spectral ranges and to quantify the associated errors. The fitting uncertainties of the retrieved  $\text{NO}_2$  SCDs were less than 3% in the UV2 channel and 1% in the VIS1 channel, and excellent agreement within a few percent was found when compared with the known  $\text{NO}_2$  concentration in the gas cell. From simultaneous  $\text{NO}_2$  SCD retrievals from adjoining spatial rows, the consistency of the results in different viewing directions (different rows of the CCD detector) was also tested. Small differences of less than 3% were found, which are probably caused by instrument effects like imperfect description of the instrument function. Finally, the SNR is characterized for EMI in-orbit measurements to better understand the instrument's performance in relation to trace gas retrievals by using two methods. Method 1 is based on the DOAS fitting residuals and radiance simulated by an RTM model. The calculated in-orbit SNR is found to be within the range of  $\sim 1000$ – $1400$  for the UV2 channel and  $\sim 1100$ – $1800$  for the VIS1 channel. These values probably underestimate the true SNR by up to about 15% due to discrepancies of the simulated radiance from the true radiance for the measurements of scattered sunlight close to the horizon. Method 2 is based on the instrumental parameters and the radiance simulated by the RTM. The SNR obtained by method 2 is almost a factor of 2 larger than that obtained by method 1, which is mostly attributed to the neglect of other instrumental sources of noise in addition to the photon noise. The estimated EMI in-orbit SNR is expected to allow retrieving  $\text{NO}_2$  SCDs with a high precision.

In general, a good performance of the EMI is shown by the on-ground measurements. The obtained results will be used for comparison with the near-future in-orbit performance after the scheduled launch in autumn 2017. Further optimization of retrieval settings (e.g., fitting wavelength range, trace gas cross sections, and ring effect) for the EMI  $\text{NO}_2$  product will be done during the inflight calibration phase after launch. Based on the results from the presented on-ground measurements, EMI is capable of monitoring the global distribution of  $\text{NO}_2$  with accuracies and precisions better than 3%, at enhanced pollution levels (as high as  $1.40 \times 10^{17}$  molecules/ $\text{cm}^2$ ), for the tested wavelength ranges (338–370 and 435–490 nm). Here, it should be noted that these results are only representative of the central part of the swath ( $-10^\circ$  to  $16^\circ$ ). Typically, the measurement uncertainties increase toward the swath edges. Thus, our results should be seen as a lower limit for measurements outside the measured viewing angle range. Although this paper focuses on the  $\text{NO}_2$  retrieval, we could expect a similar range of retrieval accuracies and precisions to be achieved by spectral analyses for similar products (e.g.,  $\text{O}_3$ ,  $\text{HCHO}$ , and  $\text{SO}_2$ ), based on the experiences from precedent satellite observations such as OMI.

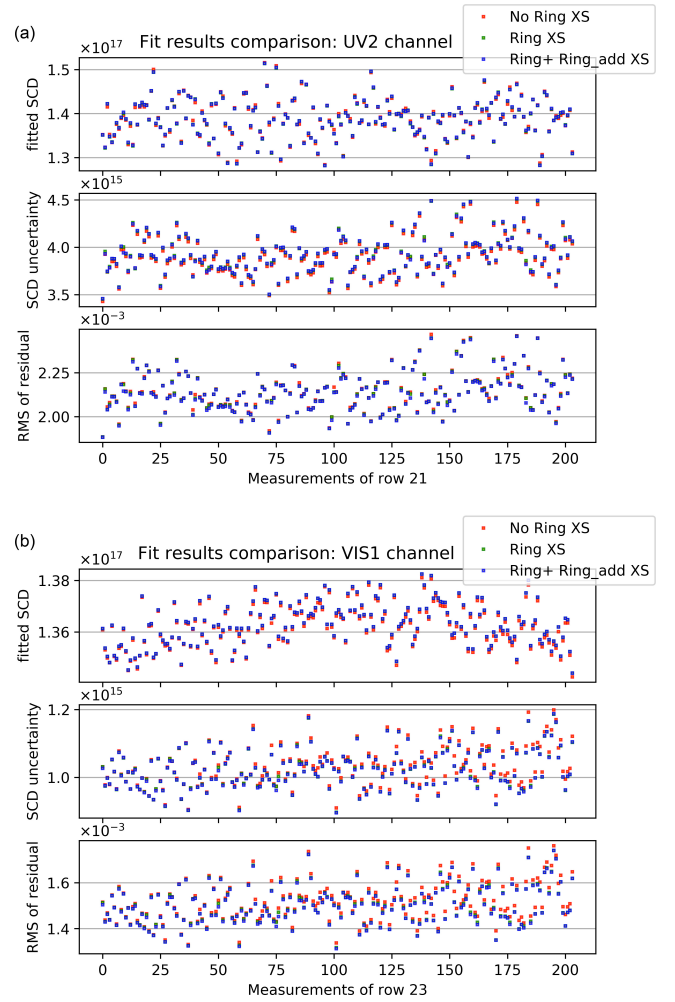


Fig. 5. Comparison plots of DOAS fitting results by using three different configurations including two ring spectra (blue), only ring spectrum (green), or no ring spectrum (red), for the (a) UV2 and (b) VIS1 channels.

## APPENDIX A TESTS ON RING EFFECT

Sensitivity tests on the effect of ring spectra on the DOAS analysis have been done before the discussion on the presented fitting results. The DOAS analyses with one and two ring spectra and without any ring spectra were performed and compared for the scattered sunlight spectra (with the gas cell filled with  $\text{NO}_2$ ). As shown from Fig. 5, it is obvious that adding one ring or two ring spectra does not affect DOAS fitting results (i.e., fit  $\text{NO}_2$  SCDs, SCD uncertainties, and root mean square of residual) significantly for both UV2 and VIS1 channels. The mean relative differences of retrieved SCD among those results are very small, less than  $5 \times 10^{-4}$  for UV2 channel and  $1 \times 10^{-3}$  for VIS1 channel, respectively.

## APPENDIX B PHOTON SHOT NOISE

To verify the photon shot noise assumption, i.e., EMI is dominated by photon shot noise, we did an additional test based on about 200 scattered sunlight spectra (with the gas



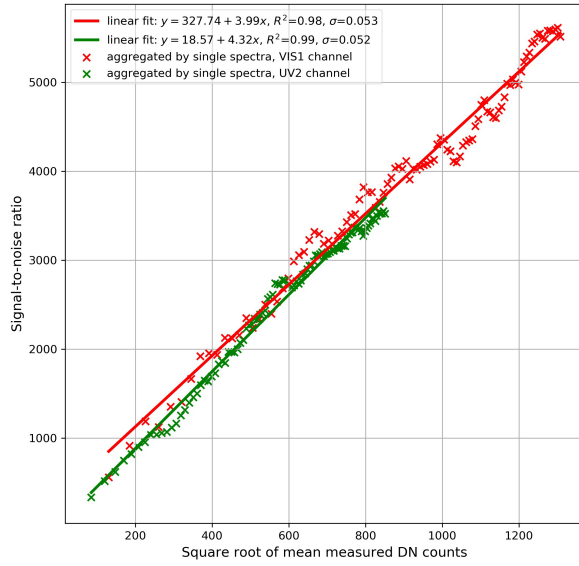


Fig. 6. Correlation plot between the SNR and the square root of the measured counts for the scattered sunlight spectra for the central CCD row with  $N_2$  in the glass cell (for details see text). Green line indicates the results for the UV2, and red line indicates the results for the VIS1 channel.

cell filled with  $N_2$ ) taken in the laboratory experiment within about 7 min.

The counts measured by the spectrometer are a function of the number of photoelectrons  $N_e$

$$\text{counts} = N_e \times f. \quad (\text{B1})$$

Here,  $f$  is the conversion factor of photoelectrons to counts.

The SNR of the measured spectra can be determined from the SD of the counts (STD) divided by the number of counts

$$\text{SNR} = \frac{\text{counts}}{\text{STD}}. \quad (\text{B2})$$

If the photon noise is only considered, then the  $\text{SNR}_{\text{photon}}$  can be calculated as

$$\text{SNR}_{\text{photon}} = \frac{N_e}{\sqrt{N_e}}. \quad (\text{B3})$$

Inserting (B1) into (B3), we obtain

$$\text{SNR}_{\text{photon}} = \sqrt{\text{counts}} \frac{1}{\sqrt{f}}. \quad (\text{B4})$$

If the noise of the measured spectra is dominated by the photon shot noise, namely,  $\text{SNR} = \text{SNR}_{\text{photon}}$ , a linear dependence of the SNR on the  $(\text{counts})^{1/2}$  is expected based on (B4). Following the theory, the SNR of spectra at different count levels is calculated and plotted against  $(\text{counts})^{1/2}$  in Fig. 6. Because all 200 spectra are measured with the same exposure time, and the intensity of the scattered sunlight was rather constant during the measurement period of about 7 min, similar count levels are reached for all spectra.

In order to calculate the SNR as a function of the count level, different numbers of single spectra are co-added. In order to minimize the effects of the slightly changing intensity of the scattered sunlight, the spectra were co-added by odd and even indices of the records, respectively. Then, the SD

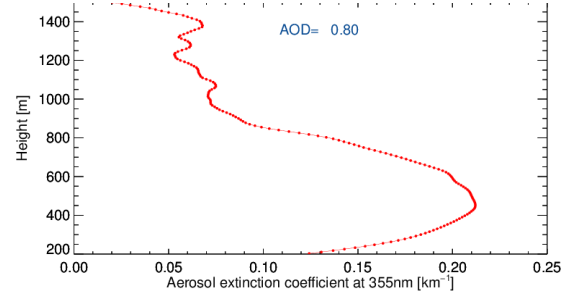


Fig. 7. Vertical profile of the aerosol extinction coefficient  $[\text{km}^{-1}]$  at 355 nm at altitudes between 0.2 and 1.5 km, averaged from LiDAR measurements during noon time of typical sunny winter days in December 2014 at the top of the AIOFM building.

of the difference between two spectra (even and odd) for different count levels is calculated. Fig. 6 indicates that the SNR depends linearly on  $\sqrt{\text{counts}}$  with a Pearson correlation coefficient  $R^2$  greater than 0.98. Note that the slopes in the plot represent the conversion factor term in the above equations. Therefore, we conclude that the measurement noise is dominated by the photon shot noise.

## APPENDIX C AEROSOL PROFILE INFORMATION

See Fig. 7.

### ACKNOWLEDGMENT

The authors would like to thank S. Beirle, Max Planck Institute for Chemistry, Mainz, Germany, for his helpful comments and suggestions during the preparation of this manuscript.

### REFERENCES

- [1] A. C. Vandaele *et al.*, "Measurements of the  $\text{NO}_2$  absorption cross-section from 42000  $\text{cm}^{-1}$  to 10000  $\text{cm}^{-1}$  (238–1000 nm) at 220 K and 294 K," *J. Quant. Spectrosc. Radiat. Transf.*, vol. 59, nos. 3–5, pp. 171–184, 1998.
- [2] Q. L. Kleipool, M. R. Dobber, J. F. de Haan, and P. F. Levelt, "Earth surface reflectance climatology from 3 years of OMI data," *J. Geophys. Res.-Atmos.*, vol. 113, no. D18, p. D18308, Sep. 2008.
- [3] H. Bovensmann *et al.*, "SCIAMACHY: Mission objectives and measurement modes," *J. Atmos. Sci.*, vol. 56, no. 2, pp. 127–150, Jan. 1999.
- [4] J. P. Burrows *et al.*, "The Global Ozone Monitoring Experiment (GOME): Mission concept and first scientific results," *J. Atmos. Sci.*, vol. 56, no. 2, pp. 151–175, Jan. 1999.
- [5] J. Callies, E. Corpaccioli, M. Eisinger, A. Hahne, and A. Lefebvre, "GOME-2—Metop's second-generation sensor for operational ozone monitoring," *ESA Bull.*, vol. 102, no. 102, pp. 28–36, May 2000.
- [6] P. F. Levelt *et al.*, "The ozone monitoring instrument," *IEEE Trans. Geosci. Remote Sens.*, vol. 44, no. 5, pp. 1093–1101, May 2006.
- [7] R. Munro *et al.*, "GOME-2 on MetOp," in *Proc. EUMETSAT Meteorol. Satellite Conf.*, vol. 1216. Helsinki, Finland, 2006, p. 48.
- [8] S. Beirle, K. F. Boersma, U. Platt, M. G. Lawrence, and T. Wagner, "Megacity emissions and lifetimes of nitrogen oxides probed from space," *Science*, vol. 333, no. 6050, pp. 1737–1739, Sep. 2011.
- [9] V. E. Fioletov *et al.*, "A global catalogue of large  $\text{SO}_2$  sources and emissions derived from the Ozone Monitoring Instrument," *Atmos. Chem. Phys.*, vol. 16, no. 18, pp. 11497–11519, Sep. 2016.
- [10] C. Leue, M. Wenig, T. Wagner, O. Klimm, U. Platt, and B. Jähne, "Quantitative analysis of  $\text{NO}_x$  emissions from Global Ozone Monitoring Experiment satellite image sequences," *J. Geophys. Res.-Atmos.*, vol. 106, no. D6, pp. 5493–5505, Mar. 2001.

- [11] F. Liu, S. Beirle, Q. Zhang, S. Dörner, K. He, and T. Wagner, "NO<sub>x</sub> lifetimes and emissions of cities and power plants in polluted background estimated by satellite observations," *Atmos. Chem. Phys.*, vol. 16, no. 8, pp. 5283–5298, 2016.
- [12] R. J. Pope *et al.*, "Evaluation of a regional air quality model using satellite column NO<sub>2</sub>: Treatment of observation errors and model boundary conditions and emissions," *Atmos. Chem. Phys.*, vol. 15, no. 10, pp. 5611–5626, 2015.
- [13] J. R. Ziemke *et al.*, "Assessment and applications of NASA ozone data products derived from Aura OMI/MLS satellite measurements in context of the GMI chemical transport model," *J. Geophys. Res.-Atmos.*, vol. 119, no. 9, pp. 5671–5699, May 2014.
- [14] K. Chance and R. L. Kurucz, "An improved high-resolution solar reference spectrum for earth's atmosphere measurements in the ultraviolet, visible, and near infrared," *J. Quant. Spectrosc. Radiat. Transf.*, vol. 111, no. 9, pp. 1289–1295, 2010.
- [15] I. Gómez, M. J. Marín, F. Pastor, and M. J. Estrela, "Improvement of the Valencia region ultraviolet index (UVI) forecasting system," *Comput. Geosci.*, vol. 41, pp. 72–82, Apr. 2012.
- [16] F. L. Herron-Thorpe, B. K. Lamb, G. H. Mount, and J. K. Vaughan, "Evaluation of a regional air quality forecast model for tropospheric NO<sub>2</sub> columns using the OMI/Aura satellite tropospheric NO<sub>2</sub> product," *Atmos. Chem. Phys.*, vol. 10, no. 18, pp. 8839–8854, 2010.
- [17] T. Wagner, S. Beirle, and T. Deutschmann, "Three-dimensional simulation of the Ring effect in observations of scattered sun light using Monte Carlo radiative transfer models," *Atmos. Meas. Techn.*, vol. 2, no. 1, pp. 113–124, 2009.
- [18] U. Platt and J. Stutz, "Differential absorption spectroscopy," in *Differential Optical Absorption Spectroscopy*. Heidelberg, Germany: Springer, 2008, pp. 135–174.
- [19] J. P. Burrows *et al.*, "Atmospheric remote-sensing reference data from GOME: Part 1. Temperature-dependent absorption cross-sections of NO<sub>2</sub> in the 231–794 nm range," *J. Quant. Spectrosc. Radiat. Transf.*, vol. 60, no. 6, pp. 1025–1031, 1998.
- [20] J. P. Burrows *et al.*, "Atmospheric remote-sensing reference data from GOME—2. Temperature-dependent absorption cross sections of O<sub>3</sub> in the 231–794 nm range," *J. Quant. Spectrosc. Radiat. Transf.*, vol. 61, no. 4, pp. 509–517, 1999.
- [21] S. R. Aliwell *et al.*, "Analysis for BrO in zenith-sky spectra: An intercomparison exercise for analysis improvement," *J. Geophys. Res.-Atmos.*, vol. 107, no. D14, pp. ACH 10-1–ACH 10-20, Jul. 2002.
- [22] R. C. Levy *et al.*, "The Collection 6 MODIS aerosol products over land and ocean," *Atmos. Meas. Techn.*, vol. 6, no. 11, pp. 2989–3034, 2013.
- [23] K. Bogumil *et al.*, "Measurements of molecular absorption spectra with the SCIAMACHY pre-flight model: Instrument characterization and reference data for atmospheric remote-sensing in the 230–2380 nm region," *J. Photochem. Photobiol. A, Chem.*, vol. 157, nos. 2–3, pp. 167–184, 2003.
- [24] X. Liu, P. K. Bhartia, K. Chance, R. J. D. Spurr, and T. P. Kurosu, "Ozone profile retrievals from the Ozone Monitoring Instrument," *Atmos. Chem. Phys.*, vol. 10, no. 5, pp. 2521–2537, 2010.
- [25] W. Chehade *et al.*, "Temperature dependent ozone absorption cross section spectra measured with the GOME-2 FM3 spectrometer and first application in satellite retrievals," *Atmos. Meas. Techn.*, vol. 6, no. 7, pp. 1623–1632, 2013.
- [26] M. Dobber, R. Dirksen, R. Voors, G. H. Mount, and P. Levelt, "Ground-based zenith sky abundances and *in situ* gas cross sections for ozone and nitrogen dioxide with the Earth Observing System Aura Ozone Monitoring Instrument," *Appl. Opt.*, vol. 44, no. 14, pp. 2846–2856, May 2005.
- [27] R. Dirksen, M. Dobber, R. Voors, and P. Levelt, "Prelaunch characterization of the Ozone Monitoring Instrument transfer function in the spectral domain," *Appl. Opt.*, vol. 45, no. 17, pp. 3972–3981, Jun. 2006.
- [28] B. Veihelmann and Q. Kleipool. (2006). *Reducing Along-Track Stripes in OMI-Level 2 Products*. Accessed: May 27, 2017. [Online]. Available: [http://disc.sci.gsfc.nasa.gov/Aura/data-holdings/OMI/documents/v003/RD08\\_TN785\\_i1\\_Reducing\\_AlongTrack\\_Stripes.pdf](http://disc.sci.gsfc.nasa.gov/Aura/data-holdings/OMI/documents/v003/RD08_TN785_i1_Reducing_AlongTrack_Stripes.pdf)
- [29] X. Prieto-Blanco, C. Montero-Orille, B. Couce, and R. de la Fuente, "Analytical design of an Offner imaging spectrometer," *Opt. Exp.*, vol. 14, no. 20, pp. 9156–9168, Oct. 2006.
- [30] C. Caspar and K. Chance, "GOME wavelength calibration using solar and atmospheric spectra," *Eur. Space Agency-Publications-ESA SP*, vol. 414, pp. 609–614, Mar. 1997.
- [31] M.-J. Zhao, F.-Q. Si, Y. Jiang, H.-J. Zhou, S.-M. Wang, and W.-Q. Liu, "In-lab calibration of space-borne differential optical absorption spectrometer," *Opt. Precis. Eng.*, vol. 21, no. 3, pp. 567–574, 2013.
- [32] S. Beirle, J. Lampel, C. Lerot, H. Sihler, and T. Wagner, "Parameterizing the instrumental spectral response function and its changes by a super-Gaussian and its derivatives," (in English), *Atmos. Meas. Techn.*, vol. 10, no. 2, pp. 581–598, Feb. 2017.
- [33] M. Zhao *et al.*, "Effect of AO/UV/RD exposure on spaceborne diffusers: A comparative experiment," *Appl. Opt.*, vol. 54, no. 31, pp. 9157–9166, Nov. 2015.
- [34] T. Danckaert *et al.*, "QDOAS software user manual," Belgian Inst. Space Aeronomy (BIRA-IASB), Uccle, Belgium, 2012.
- [35] A. Piders *et al.*, "The Cabauw Intercomparison campaign for Nitrogen Dioxide measuring Instruments (CINDI): Design, execution, and early results," *Atmos. Meas. Techn.*, vol. 5, no. 2, pp. 457–485, 2012.
- [36] H. K. Roscoe *et al.*, "Intercomparison of slant column measurements of NO<sub>2</sub> and O<sub>4</sub> by MAX-DOAS and zenith-sky UV and visible spectrometers," *Atmos. Meas. Techn.*, vol. 3, no. 6, pp. 1629–1646, 2010.
- [37] K. F. Boersma *et al.*, "An improved tropospheric NO<sub>2</sub> column retrieval algorithm for the Ozone Monitoring Instrument," *Atmos. Meas. Techn.*, vol. 4, no. 9, pp. 1905–1928, 2011.
- [38] K. F. Boersma *et al.*, "Near-real time retrieval of tropospheric NO<sub>2</sub> from OMI," *Atmos. Chem. Phys.*, vol. 7, no. 8, pp. 2103–2118, 2007.
- [39] E. J. Bucsela *et al.*, "A new stratospheric and tropospheric NO<sub>2</sub> retrieval algorithm for nadir-viewing satellite instruments: Applications to OMI," *Atmos. Meas. Techn.*, vol. 6, no. 10, pp. 2607–2626, 2013.
- [40] R. J. D. Spurr, "VLIDORT: A linearized pseudo-spherical vector discrete ordinate radiative transfer code for forward model and retrieval studies in multilayer multiple scattering media," *J. Quant. Spectrosc. Radiat. Transf.*, vol. 102, no. 2, pp. 316–342, Nov. 2006.
- [41] S. Donner, J. Kuhn, M. Van Roozendael, Y. Wang, and T. Wagner, "Three ways of elevation calibration of MAX-DOAS instruments during the CINDI-2 campaign," in *Proc. EGU General Assembly Conf. Abstracts*, vol. 19, 2017, p. 7514.

**Chengxin Zhang** received the B.Eng. degree from the University of Science and Technology of China, Hefei, China, in 2015, where he is currently pursuing the Ph.D. degree with the School of Earth and Space Science.

His research interests include the satellite retrieval of atmospheric trace gases such as nitrogen dioxide and ozone.



**Cheng Liu** received the Ph.D. degree in environmental physics from the University of Heidelberg, Heidelberg, Germany, in 2010.

He was a Postdoctoral Researcher at Harvard University, Cambridge, MA, USA. Since 2015, he has been a Professor with the University of Science and Technology of China, Hefei, China. His research interests include the remote sensing of air pollution gases and greenhouse gases from satellite and ground-based observations.



**Yang Wang** received the Ph.D. degree in remote sensing technology from the University of Chinese Academy of Sciences, Hefei, China, in 2014.

He is currently a Research Scientist with the Max Planck Institute for Chemistry, Mainz, Germany. His research interests include the trace gas retrieval from MAX-DOAS.





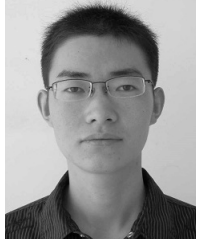
**Fuqi Si** received the Ph.D. degree from the Anhui Institute of Optics and Fine Mechanics (AIOFM), Chinese Academy of Sciences, Hefei, China, in 2006.

He was a Post-Doctoral Researcher at Chiba University, Chiba, Japan, and at Heidelberg University, Heidelberg, Germany. He is currently the Deputy Director of the Environment Optical Center, AIOFM. His research interests include the design of optical instruments.



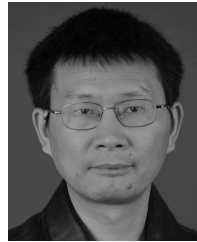
**Ka Lok Chan** received the Ph.D. degree in energy and environment from the City University of Hong Kong, Hong Kong, in 2015.

He is currently a Post-Doctoral Researcher with the University of Munich, Munich, Germany. His research interests include the remote sensing of air pollution.



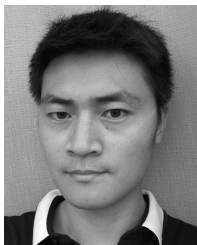
**Haijin Zhou** received the Ph.D. degree from the University of Science and Technology of China, Hefei, China.

He is currently an Associate Professor with the Anhui Institute of Optics and Fine Mechanics, Chinese Academy of Sciences, Hefei. His research interests include the design of optical instruments.



**Xiong Liu** received the Ph.D. degree in atmospheric science from The University of Alabama in Huntsville, Huntsville, AL, USA, in 2002.

He is currently a Research Scientist with the Harvard-Smithsonian Center for Astrophysics, Cambridge, MA, USA. His research interests include the remote sensing of atmospheric trace gases, aerosols, and clouds, data validation, and analysis.



**Minjie Zhao** received the Ph.D. degree in precision instrument and machinery from the Anhui Institute of Optics and Fine Mechanics (AIOFM), Chinese Academy of Sciences, Hefei, China, in 2016.

He is currently an Assistant Professor with AIOFM. His research interests include the design of optical instruments.



**Pinhua Xie** received the Ph.D. degree from the Anhui Institute of Optics and Fine Mechanics (AIOFM), Chinese Academy of Sciences, Hefei, China, in 2002.

She is currently the Deputy Director of AIOFM. Her research interests include the optical measurement techniques for atmospheric trace gas detection.



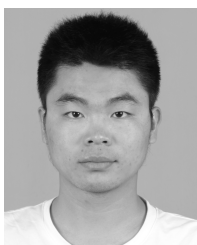
**Wenjing Su** received the B.S. degree in atmospheric science from the University of Science and Technology of China, Hefei, China, in 2016, where she is currently pursuing the M.S. degree with the School of Earth and Space Science.

Her research interests include the remote sensing of air pollution.



**Jianguo Liu** received the Ph.D. degree from the Anhui Institute of Optics and Fine Mechanics, Chinese Academy of Sciences, Hefei, China, in 1999.

He is currently the Deputy President of the Hefei Institutes of Physical Science, Chinese Academy of Sciences, Hefei, and also the Director of the Key Laboratory of Environmental Optics and Technology. His research interests include the optical environment pollution monitoring technology.



**Wenqiang Zhang** received the B.S. degree in environmental engineering from the University of Electronic Science and Technology of China, Chengdu, China, in 2016. He is currently pursuing the M.S. degree with the School of Environmental Science and Optoelectronic Technology, University of Science and Technology of China, Hefei, China.

His research interests include the remote sensing of air pollution.



**Thomas Wagner** received the Ph.D. degree in physics from the University of Heidelberg, Heidelberg, Germany, in 1999.

Since 2006, he has been an extraordinary Professor with the University of Heidelberg. In 2006, he joined the Max Planck Institute for Chemistry, Mainz, Germany, where he is currently leading the research group on satellite remote sensing. His research interests include remote sensing of atmospheric trace gases and aerosols from ground-based and satellite observations in the UV and visible spectral ranges.